small structures
www.small-structures.com

Chemically Tailored Semiconductor Moiré Superlattices of Janus Heterobilayers

Wenjin Zhang, Zheng Liu, Hiroshi Nakajo, Soma Aoki, Haonan Wang, Yanlin Wang, Yanlin Gao, Mina Maruyama, Takuto Kawakami, Yasuyuki Makino, Masahiko Kaneda, Tongmin Chen, Kohei Aso, Tomoya Ogawa, Takahiko Endo, Yusuke Nakanishi, Kenji Watanabe, Takashi Taniguchi, Yoshifumi Oshima, Yukiko Yamada-Takamura, Mikito Koshino, Susumu Okada, Kazunari Matsuda, Toshiaki Kato,* and Yasumitsu Miyata**

Janus monolayers of transition metal dichalcogenides (TMDCs) are promising building blocks for moiré superlattices because of their built-in electric field and clean fabrication process. In particular, Janus TMDC monolayers can be chemically converted from conventional TMDC monolayers by atomic substitution, enabling the direct formation of lattice-mismatched heterobilayers from TMDC bilayers. However, the moiré superlattices of Janus heterobilayers have not been studied experimentally. Herein, this work reports the fabrication and characterization of semiconductor moiré superlattices in chemically tailored Janus heterobilayers. The $MoSSe/MoSe_2$ (or $WSSe/WSe_2$) Janus heterobilayers are prepared by replacing the top layer Se atoms with S atoms in $MoSe_2$ (or WSe_2) bilayer using H_2 plasma treatment. Scanning transmission electron microscopy reveals that an average moiré period of about 14 nm formed due to lattice mismatch resulting from the chalcogen substitutions. The cryogenic photoluminescence spectra show sharp, near-infrared emissions, which are attributed to excitons trapped by moiré potentials based on comparison with theoretical calculations. The Janus-based heterostructures provide a long-period moiré system with built-in potential even for nontwisted heterobilayers, allowing the functionalization of confined and correlated electron systems.

1. Introduction

Moiré superlattices, which arise from a lattice mismatch or relative twist angle between two different layers, have recently emerged as an ideal platform for exploring exotic quantum phenomena and future applications of two-dimensional (2D) materials. Nanoscale periodic potential in moiré superlattices provides a new degree of freedom for tuning and studying the flat band effect and correlated physics.[1–6] To date, moiré superlattices have been fabricated using a variety of 2D materials, including graphene, hexagonal boron nitride (hBN), and transition metal dichalcogenides (TMDCs). Among these, Janus monolayers of TMDCs (represented as MXY (M = Mo and W; X, Y = S, Se, and Te)) provide an additional degree of freedom in moiré superlattices. Janus monolayers have two different chalcogen atoms above and below the central metal atom, and because of this asymmetric structure, they have a built-in

W. Zhang, Y. Makino, M. Kaneda, T. Ogawa, T. Endo, Y. Nakanishi, Y. Miyata
Department of Physics
Tokyo Metropolitan University
Hachioji 192-0397, Japan
E-mail: wjzhang@tmu.ac.jp; ymiyata@tmu.ac.jp

Z. Liu
Innovative Functional Materials Research Institute
National Institute of Advanced Industrial Science and Technology (AIST)
Nagoya 463-8560, Japan

The ORCID identification number(s) for the author(s) of this article can be found under https://doi.org/10.1002/sstr.202300514.

DOI: 10.1002/sstr.202300514

H. Nakajo, S. Aoki, T. Kato
Graduate School of Engineering
Tohoku University
Sendai 980-8579, Japan
E-mail: kato12@tohoku.ac.jp

H. Nakajo, S. Aoki, T. Kato
Advanced Institute for Materials Research (AIMR)
Tohoku University
Sendai 980-8577, Japan

H. Nakajo
KOKUSAI ELECTRIC CORP.
Toyama 939-2393, Japan

H. Wang, Y. Wang, K. Matsuda
Institute of Advanced Energy
Kyoto University
Kyoto 611-0011, Japan

out-of-plane electric field.[7] Recent theoretical studies have predicted that this asymmetric structure leads to various properties, such as large Rashba spin-orbit coupling,[8–15] piezoelectricity,[16] nonlinear optical response,[17,18] and long-lived charge transfer excitons.[10,11,19–25] Furthermore, the excitons in Janus heterobilayer moiré superlattices have been calculated to realize a high-temperature Bose–Einstein condensation state as a result of the built-in electric field that enhances the exciton lifetime and the repulsive interactions between trapped excitons.[23]

In addition to these theoretical works, recent advances in surface-chalcogen exchange techniques have experimentally realized Janus monolayers, such as MoSSe and WSSe, from the corresponding monolayer TMDCs.[26–34] This technique has been applied to the direct preparation of Janus heterobilayers, including $WSSe/WSe_2$ from bilayer WSe_2.[35–37] The WSSe/MoSSe heterobilayer was also obtained by the transfer process.[36,37] These advances allow us to access their excitonic properties. Previous reports demonstrated ultrafast charge transfer and enhanced interlayer coupling effects in Janus heterobilayers.[35,37,38] However, the moiré superlattices of Janus heterobilayers are still unknown experimentally. Notably, the MSSe monolayers have an intermediate lattice constant between MS_2 and MSe_2.[7,26] This small lattice mismatch enables the formation of long-period moiré superlattices even from nontwisted bilayers in Janus heterobilayers. Such a long moiré period compared to conventional nontwisted heterobilayers could be useful for further tuning the electron correlation in moiré superlattices. In addition, the direct preparation of Janus heterobilayers provides a method to fabricate scalable moiré superlattices from MX_2 bilayers with thermodynamically stable configurations such as Bernal stacking.

Here, we present the fabrication and characterization of moiré superlattices in Janus heterobilayers of $MoSSe/MoSe_2$ and $WSSe/WSe_2$. Janus heterobilayers were prepared from bilayer $MoSe_2$ (or WSe_2) using plasma functionalization and were characterized by Raman and photoluminescence (PL) measurements. Nanoscale moiré structures were visualized using electron microscopy observations. Furthermore, their excitonic properties were investigated using cryogenic PL spectroscopy together with theoretical calculations.

Y. Gao, M. Maruyama, S. Okada
Department of Physics
Graduate School of Pure and Applied Sciences
University of Tsukuba
Tsukuba 305-8571, Japan

T. Kawakami, M. Koshino
Department of Physics
Osaka University
Toyonaka, Osaka 560-0043, Japan

T. Chen, K. Aso, Y. Oshima, Y. Yamada-Takamura
School of Materials Science
Japan Advanced Institute of Science and Technology (JAIST)
Ishikawa 923-1292, Japan

K. Watanabe
Research Center for Electronic and Optical Materials
NIMS
Tsukuba 305-0044, Japan

T. Taniguchi
Research Center for Materials Nanoarchitectonics
NIMS
Tsukuba 305-0044, Japan

2. Results and Discussion

2.1. Preparation and Structure Analysis of Janus Heterobilayer

We first synthesized bilayer MSe_2 (M = Mo and W) on SiO_2/Si substrates using chemical vapor deposition (CVD). Then, the top surface Se atoms were substituted by S atoms using H_2 plasma treatment (**Figure 1**a). We note that the S substitution was also confirmed by high-resolution elemental mapping in our previous study.[39] As a result, the transition metal atoms (M) were covalently bonded to the top S and underlying Se atoms within the top layer, resulting in the formation of $MSSe/MSe_2$ heterobilayers. Owing to the smaller lattice constant of the upper Janus monolayers, the present process leads to the formation of moiré superlattices from nontwisted bilayer MSe_2, as shown in Figure 1b.

Figure 1c shows an optical microscopy image of a grain composed of monolayer and bilayer regions after the plasma treatment. The optical image shows stacked triangular grains of different sizes. The same orientation of the triangles suggests the formation of 3R-like stacking.[40,41] Notably, 2H- and 3R-like stacking were randomly observed in the present CVD-grown samples (Figure S1, Supporting Information). Following the plasma treatment, the conversion from $MoSe_2$ to MoSSe was confirmed from room-temperature PL/Raman intensity maps and spectra (Figure 1d–h and S2, Supporting Information). Figure 1d,e shows the A_1' mode Raman intensity maps of MoSSe at $290\,cm^{-1}$ and $MoSe_2$ at $240\,cm^{-1}$. The A_1' mode at $290\,cm^{-1}$ in Figure 1g is consistent with that of MoSSe in the previous study.[42] The Raman signal of MoSSe can be seen throughout the region of the triangular grain, while that of $MoSe_2$ is only observed in the bilayer region. This indicates that the surface Se atoms were uniformly substituted by S atoms, and in the bilayer region, the bottom $MoSe_2$ was protected from the substitution reaction. As shown in Figure 1g, in the bilayer region, the A'_1 mode of MoSSe at $290\,cm^{-1}$ had comparable intensity to the A'_1 mode of $MoSe_2$ at $240\,cm^{-1}$, whereas only the A'_1 mode at $240\,cm^{-1}$ was observed in the pristine bilayer $MoSe_2$. For the PL intensity map (Figure 1f), the bilayer region shows weak PL intensity at 1.69 eV compared to the monolayer region. The PL spectra of the $MoSSe/MoSe_2$ showed two typical peaks corresponding to MoSSe (1.65 eV) and $MoSe_2$ (1.47 eV), which differed from that of the bilayer $MoSe_2$ before the plasma treatment (Figure 1h). The PL peak at 1.65 eV was also consistent with the reported spectra of monolayer MoSSe.[26] Similar changes in Raman and PL spectra were observed in the monolayer region (Figure S2, Supporting Information). We note that these Raman and PL peaks of MoSSe differ from those of the intermediate partially substituted Janus structure and metallic state of MoSH[28,43,44] and random alloyed $MoS_{2x}Se_{2(1-x)}$ monolayer, which shows multiple peaks including both MoS_2 and $MoSe_2$ derived Raman modes.[45,46] The present plasma treatment was also applied to fabricate the $WSSe/WSe_2$ samples (Figure S3,and S4, Supporting Information).

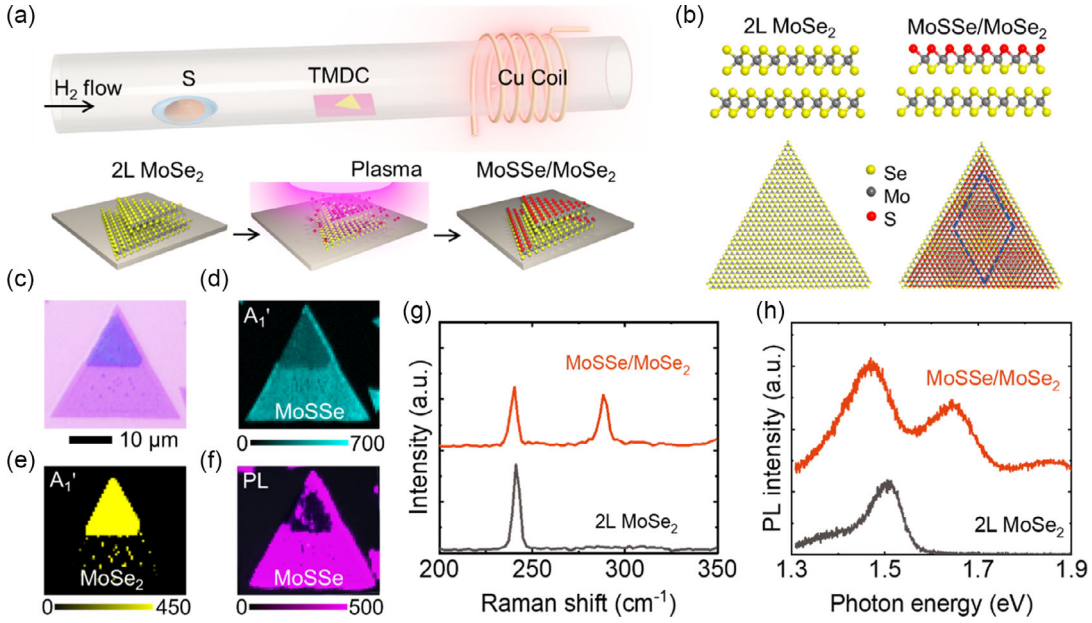

Figure 1. Fabrication and optical characterization of $MoSSe/MoSe_2$ heterobilayer. a) Schematic of the experimental setup and the conversion process from bilayer (2 L) $MoSe_2$ to heterobilayer $MoSSe/MoSe_2$ using H_2 plasma treatment. b) Side and top views of bilayer $MoSe_2$ and Janus heterobilayer $MoSSe/MoSe_2$. The periodic moiré superlattice is visualized by changing the lattice constant of the top layer. The blue-dashed shape indicates a moiré unit cell. c) Typical optical microscope image of the heterobilayer $MoSSe/MoSe_2$ prepared on a SiO_2/Si substrate. Raman intensity map of A_1' mode of d) MoSSe at 290 cm^{-1} and e) $MoSe_2$ at 240 cm^{-1}. f) PL intensity map of MoSSe (1.69 eV). g) Raman and h) PL spectra of the bilayer $MoSe_2$ and heterobilayer $MoSSe/MoSe_2$.

2.2. Atomic Structure of Janus $MoSSe/MoSe_2$ Heterobilayer

The atomic arrangement of Janus heterobilayers was investigated using scanning transmission electron microscopy (STEM). **Figure 2**a shows the high-angle annular dark-field (HAADF) STEM image of $MoSSe/MoSe_2$. Figure 2b shows the enlarged images of the four regions labeled i–iv in Figure 2a. Images i and iv can be assigned to R_h^h stacking, whereas the images ii and iii correspond to R_h^X and R_h^M stacking, respectively (Figure 2d). The R_h^h stacking shows simple honeycomb lattices, which are displayed in Figure 2a as lighter contrasts. In this region, the distance of the moiré pattern, a_M, is about 16 nm. Figure 2e shows the fast Fourier transform (FFT) pattern obtained from Figure 2a, and presents the sixfold symmetry of the spots. Notably, when each spot was magnified, two distinct peaks were observed (Figure 2e). The inner and outer spots were assigned to the FFT patterns of the honeycomb lattices of $MoSe_2$ and MoSSe with the same orientation, respectively. From the peak distances, the lattice mismatch between the MoSSe and $MoSe_2$ monolayers was estimated to be 2.1% in this region. The lattice constant of MoSSe can be estimated to be 0.321 nm by using that of $MoSe_2$ (0.328 nm). This lattice mismatch, δ, corresponds to a moiré period of 15.4 nm, based on the relation of $a_M \approx \frac{a_{MoSSe}}{\delta}$.[2,47] Using the obtained lattice

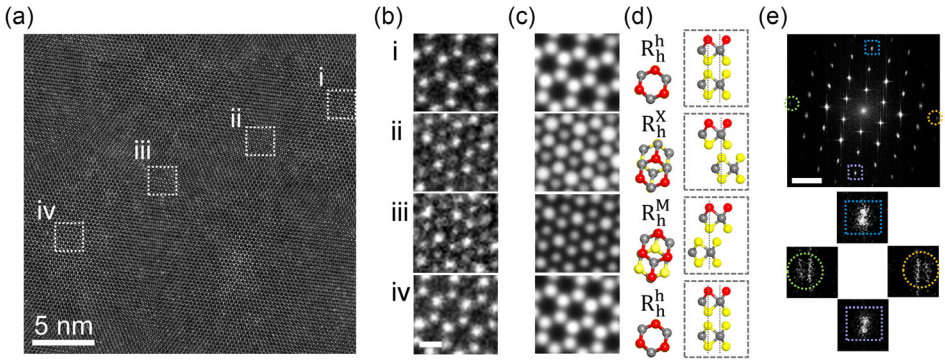

Figure 2. Atomic structure of the moiré superlattice in the Janus heterobilayer $MoSSe/MoSe_2$. a) HAADF-STEM image of $MoSSe/MoSe_2$. b) Enlarged and c) simulated images of the selected regions from (a), and the scale bar is 0.25 nm. d) The schematics show the top and side views with a periodic stacking

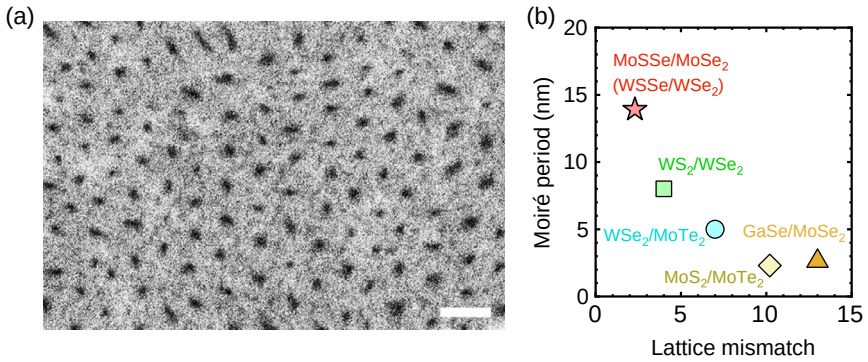

Figure 3. Wide-field moiré patterns of the heterobilayer $MoSSe/MoSe_2$. a) ABF-STEM image of the $MoSSe/MoSe_2$ heterobilayer on the TEM grid. Scale bar is 20 nm. b) Relationship between the moiré period and the lattice mismatch for five nontwisted (or nearzero twist angle) heterobilayers including $MoSSe/MoSe_2$ ($WSSe/WSe_2$) in the present work, $MoTe_2/MoS_2$, WS_2/WSe_2, $GaSe/MoSe_2$, and $WSe_2/MoTe_2$ nontwisted heterobilayers.[48–51].

parameters, we simulated the HAADF-STEM images. As shown in Figure 2b,c, the experimental images are in good agreement with the simulated ones of the structure model in Figure 2d.

Figure 3a shows the wide-area annular bright-field (ABF) STEM image of the $MoSSe/MoSe_2$ heterobilayer. Here, we show the ABF STEM image due to its high contrast, and the contrast of the moiré patterns between the ABF and HAADF–STEM images was reversed (Figure S5, Supporting Information). The black dots correspond to the moiré patterns. The distance between two adjacent black dots ranges from 12 nm to 17 nm, and the average moiré period was 13.9 ± 0.5 nm. The lattice mismatch and the MoSSe lattice constant were estimated to be around 2.3% and 0.320 nm using the equation, $a_M \approx \frac{a_{MoSSe}}{\delta}$, respectively. These values are close to those obtained from the local region, as shown in Figure 2, and were consistent with the lattice constant of previous experimental and theoretical works[13,26,33] This result also supports uniform conversion of the top layers by the present plasma treatment. We note that the inhomogeneity of moiré patterns can be explained by the introduction of in-plane tensile strain into the MoSSe during the conversion from $MoSe_2$ (Figure S5, Supporting Information). We also observed similar moiré structures in the $WSSe/WSe_2$ Janus heterobilayer (Figure S6, Supporting Information). Notably, due to their small lattice mismatch, the $MoSSe/MoSe_2$ and $WSSe/WSe_2$ heterobilayers have longer moiré period compared to other nontwisted (or nearzero twist angle) heterobilayers, such as $MoTe_2/MoS_2$, WS_2/WSe_2, $GaSe/MoSe_2$, and $WSe_2/MoTe_2$ (Figure 3b).[48–51]

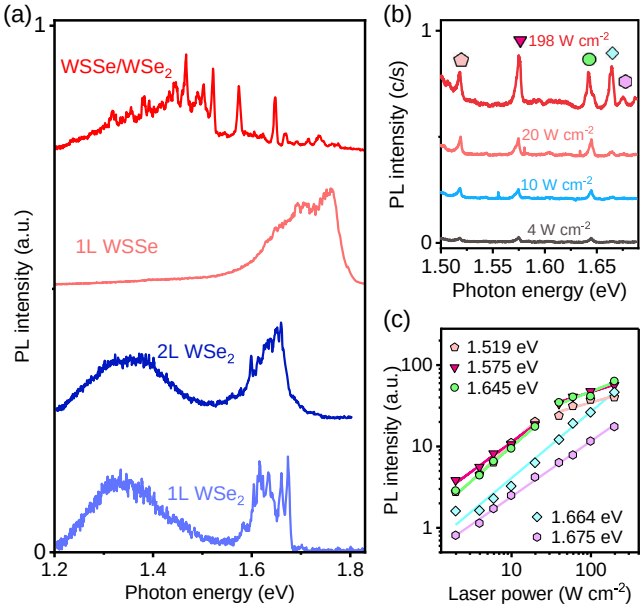

Figure 4. Moiré excitons in the Janus heterobilayer $WSSe/WSe_2$. a) PL spectra of hBN-encapsulated (red) heterobilayer $WSSe/WSe_2$, (pink) monolayer (1 L) Janus WSSe, (blue) bilayer (2 L), and (light blue) 1 L WSe_2 measured at 8 K. b) Excitation power-dependent PL spectra and c) PL peak intensities at 1.519, 1.575, 1.645, 1.664, and 1.675 eV of the heterobilayer $WSSe/WSe_2$. A linear power dependence is observed for the peaks at 1.664 and 1.675 eV, whereas the other three peaks show a saturating behavior above 20 W cm^{-2}.

2.3. Low-Temperature PL Spectra of Janus $WSSe/WSe_2$ Heterobilayer

With the emergence of moiré structure in the present Janus heterobilayers, the nanoscale periodic moiré potentials could locally trap the excitons at low temperatures. For low-temperature PL measurement, the Janus heterobilayers were encapsulated with hBN flakes to obtain high optical quality (Figure S7, Supporting Information). In this work, we focused on the $WSSe/WSe_2$ because relatively bright PL was measured compared to the $MoSSe/MoSe_2$ in the present study. **Figure 4**a shows the PL spectra of the hBN-encapsulated WSSe monolayer and $WSSe/WSe_2$ heterobilayer at 8 K. The monolayer WSSe exhibited a broad peak between 1.6 and 1.8 eV. This broad peak resulted from a mixed contribution from defect-derived localized excitons, charged excitons, and neutral excitons.[28,34,52] By contrast, only the $WSSe/WSe_2$ heterobilayer showed multiple sharp peaks with line widths of 3–6 meV between 1.3 and 1.7 eV. These sharp peaks have never been observed for the other samples, including monolayer WSSe, monolayer and bilayer WSe_2. From this comparison, these multiple, sharp PL peaks could be attributed to

excitons trapped in the moiré potential rather than defects or lattice strain.[53,54]

We found that these multiple PL peaks have different excitation power dependence, as shown in Figure 4b. Figure 4c shows the PL intensities of different peaks plotted as a function of excitation laser power. For the three peaks below 1.645 eV, the PL intensity tends to show a saturation behavior at a relatively low excitation power density of 20 W cm^{-2}. Conversely, a linear power dependence was observed for the peaks at 1.664 and 1.675 eV. The saturation behavior is probably due to the longer lifetime of interlayer excitons than that of intralayer excitons. Owing to the staggered band alignment of WSSe/WSe_2 (shown later), interlayer excitons were expected to be formed by efficient interlayer charge transfer. Because of their long lifetimes, the interlayer excitons could easily occupy the individual moiré potentials at relatively low exciton power and show saturation behavior.

Besides the exciton types mentioned above, it should be noted that the multiple peaks are due to the inhomogeneity of moiré potential. Indeed, the PL spectra showed significant variations in different regions (Figure S8, Supporting Information). The inhomogeneous moiré patterns were observed in the STEM images (Figure 3a) and also in the previous reports.[55,56]. Such inhomogeneity is probably derived from introducing unintentional lattice strain during the plasma treatment and/or the hBN encapsulation. Further improvement of the fabrication process is also necessary to suppress the strain effect on Janus heterobilayers.

2.4. Electronic Band Structure of WSSe/WSe_2 Moiré Superlattice

To confirm the staggered band alignment, the band structures of monolayer WSSe and WSe_2 and their heterobilayer were obtained using first-principles calculations. The valence and conduction band edges of monolayer WSSe were lower than those of monolayer WSe_2 (**Figure 5**a). This suggests the formation of staggered band alignment for the heterobilayer as reported previously.[37] We found that the staggered band alignment of WSSe/WSe_2 was resilient to variations in lattice constant (Figure S9, Supporting Information). The present calculations also showed a potential difference of 0.7 V between the vacuum on the S- and Se-sides (Figure S9, Supporting Information), which was comparable to previously reported results of various Janus monolayer TMDCs.[9,15,23,57] Together with the confinement effect of the moiré potential, the staggered band alignment could lead to the formation of long-lived, interlayer excitons in the WSSe/WSe_2 heterobilayer. Evaluation of the intrinsic exciton lifetime would require highly clean and carrier-tunable devices of Janus heterobilayers, which is a future challenge.

The above first-principles calculation ignored the effect of the moiré pattern caused by a tiny difference in the lattice constants of WSSe and WSe_2. To see this, we calculated the band structure of WSSe/WSe_2 moiré superlattice using a tight binding model (See S10, Supporting Information). Here, we take the ratio in lattice constants between WSSe and WSe_2 to be 35:36, which approximates the ratio obtained by first-principle calculation (Figure 5a). Due to the large periods of the moiré superlattice, the electronic bands are folded in the mini-Brillouin zone and divided into the subband structure (Figure 5b). As shown in Figure 5c, the density of states exhibits multiple sharp peaks, which is attributed to the emergence of the subband formation. The spatial distribution of the density of states shows the long-range periodic patterns (Figure 5d). Particularly, electronic states at VBM exhibit an energetically isolated narrow band and are confined to the central region of moiré pattern where chalcogen and transition metal atoms are vertically aligned (as in the top panel of Figure 2b–d). The isolated narrow band and localized density of states support the observation of sharp PL peaks due to the formation of moiré potentials that can trap the intra- and interlayer excitons.

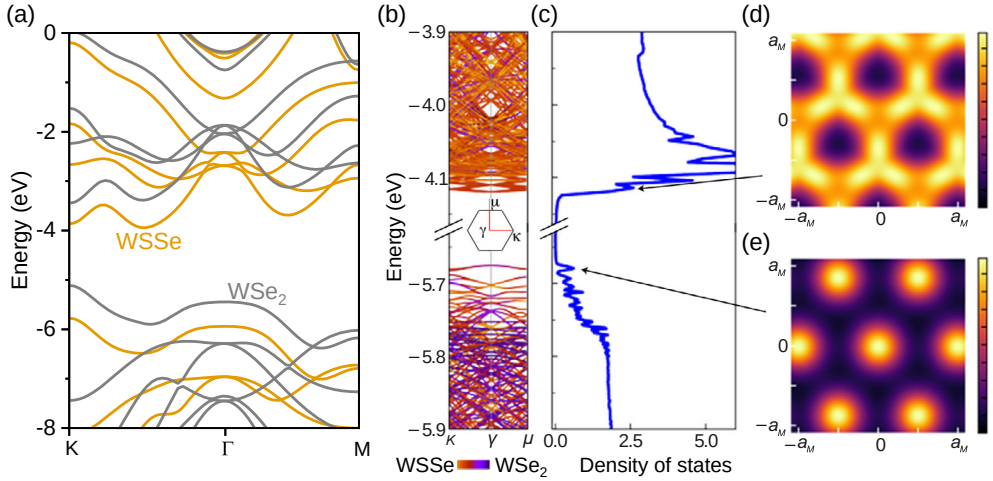

Figure 5. Electronic structures of Janus monolayer WSSe, WSe_2, and moiré superlattice of WSSe/WSe_2. a) Electronic band structures of monolayer (orange) WSSe and (gray) WSe_2 under optimized lattice constants of 3.191 and 3.28 Å calculated by first-principles calculation. b–d) Electronic structures of moiré superlattice of WSSe/WSe_2 calculated by a tight binding model. b) Band structure along the κ–γ–μ points of the mini-Brillouin zone (inset). Color code indicates the probability amplitudes of the wave function in WSSe and WSe_2 layers. c) Density of states with sharp peak structure associated with the subband formation. Local density of states at d) $E = -4.12$ eV and e) −5.68 eV, respectively. a_M is the lattice constant of moiré superlattice. Here, we take superlattice including 36 × 36 WSSe units and 35 × 35 WSe_2.

3. Conclusion

In summary, we have demonstrated the fabrication and structure/optical characterizations of moiré superlattices based on $MoSSe/MoSe_2$ and $WSSe/WSe_2$ Janus heterobilayers. These heterobilayers were prepared by plasma functionalization from bilayer TMDCs. The STEM observations visualized the moiré superlattices with an average lattice constant of about 14 nm. The moiré excitons were studied using cryogenic PL measurements together with the theoretical calculations. The staggered band alignment was confirmed by the first-principles calculations, and the formation of moiré potential was also supported by the tight-binding calculations.

The present study provides a novel way to prepare the moiré superlattices using a simple postgrowth plasma treatment at room temperature. This process enables the rapid and scalable fabrication of moiré superlattices with a clean interface from nontwisted bilayers and multilayers, which can be obtained by conventional CVD process. In terms of structural features, a small lattice mismatch of the Janus heterobilayers allows the formation of long-period moiré superlattices exceeding 10 nm in nontwisted heterobilayers. Such long-period potentials have usually been difficult to create in conventional heterobilayer TMDCs due to large lattice mismatches. It is noted that twisted "homobilayers" allow the formation of longer-period moiré structures, but cannot avoid large inhomogeneities due to small angular misalignments. In addition to the longer-period moiré structures, the built-in potential of Janus monolayers offers the possibility to modulate a wide variety of quantum phenomena, including noncentrosymmetric superconductivity, Majorana fermions, topological phases, and Bose–Einstein condensation of excitons.[23,58]

4. Experimental Section

CVD Growth of TMDCs: $MoSe_2$ and WSe_2 used in this study were grown on Si substrates with a SiO_2 thickness of 285 nm using the CVD method with two electric furnaces. For WSe_2, the substrate was set in a quartz tube with WO_3 powder (300 mg) and Se beads (3–4 g). N_2 gas with a constant flow rate of 450 sccm was used to fill the quartz tube under atmospheric pressure. The WO_3 powder was heated to 950 °C using the downstream electric furnace. When the furnace reached the target temperature, Se was heated at 380 °C for 2 min under H_2/N_2 ($H_2 = 0.7\%$) gas with a total flow rate of 450 sccm using the upstream electric furnace. Finally, the entire system was cooled using a fan. $MoSe_2$ was prepared using MoO_2 powder (80–120 mg) and heated at 870–880 °C under a mixed gas of N_2 (200–250 sccm) and H_2 (1 sccm). The Se was heated at 420 °C for 2 min.

Plasma Treatment: Janus heterobilayers were prepared by the plasma-assisted surface chemical substitution from bilayer $MoSe_2$ and WSe_2, as shown in Figure 1a.[36,39] The CVD-grown TMDC samples ($MoSe_2$ and WSe_2) were placed ($z = 300$–350 mm) in a quartz tube (diameter 20 mm and length = 600 mm), where $z = 0$ mm is the end of quartz tube in the upstream side. The quartz tube was pumped down to base pressure (≈few Pa) with a rotary pump. Then, 99.99% pure H_2 was supplied (≈20 sccm) and the tube pressure was kept at 38 Pa. S powder was placed in the upstream. A copper coil (diameter = 50 mm) was placed around the downstream ($z = 400$–500 mm) region of the quartz tube as an antenna for inductively coupled plasma generation. S powder was placed in the upstream ($z = 200$–250 mm). The radio frequency power for the copper coil was set to 15–30 W. The reaction time was adjusted between 30 and 60 min. All treatments were carried out under room temperature conditions.

hBN Encapsulation: The hBN-encapsulated samples were prepared using a typical polymer-assisted lifting and peeling process using acrylic resin stamps, as reported previously.[59] Thin hBN flakes were mechanically exfoliated onto the SiO_2/Si substrates from bulk crystals.[60] The detailed processes are presented in Figure S11, Supporting Information.

Optical Measurements: Room temperature PL spectroscopy was conducted using a Renishaw inVia spectrometer equipped with a 532 nm excitation light. Cryogenic PL was performed using a lab-made optical setup with a cryostat under vacuum conditions ($<10^{-4}$ Pa). A 635 nm continuous-wave semiconductor laser was used as the excitation source. The laser was focused using a 50× objective lens. The PL signals were collected using the same objective lens and finally detected using a cooled charge-coupled device through a spectrometer.

STEM Observations and Analyses: For the STEM observations, HAADF- and ABF-STEM images and STEM-EDS mapping were collected at room temperature using a JEM-ARM200F (Cold FEG) equipped with a CEOS ASCOR corrector and a 100 mm^2 SDD detector operated at 120 kV. The simulation of HAADF-STEM images was performed using Tempas simulation package, with parameters similar to the experimental ones.

Computational Methods: The theoretical calculations, as shown in Figure 5a, were conducted using the STATE program package,[61,62] based on density functional theory.[63,64] The exchange-correlation potential energy between electrons is approximated using the generalized gradient approximation with a Perdew–Burke–Ernzerhof functional.[65] The weak dispersive interaction between the WSe_2 and WSSe layers was treated using vdW-DF2 with the C09 exchange-correlation functional.[66,67] Ultrasoft pseudopotentials were adopted to describe the interaction between valence electrons and ions.[68] The valence wave functions and deficit charge density were expanded in terms of plane-wave basis sets with cutoff energies of 25 and 225 Ry, respectively. Brillouin-zone integration was carried out with 9 × 9 k-meshes. The lattice parameters and internal atomic coordinates were fully optimized until the force acting on the atoms was $<1.33 \times 10^{-3}$ hartree $bohr^{-1}$. To exclude the unphysical dipole interaction with the periodic images normal to the sheet, we used the effective screening medium method.[69,70] For the Janus heterobilayer calculation, the interlayer distance between WSSe and WSe_2 was 3.18 Å (Figure S9, Supporting Information).

Supporting Information

Supporting Information is available from the Wiley Online Library or from the author.

Acknowledgements

The authors acknowledge T. Tanaka and S. Furusawa for providing valuable advice and help on HAADF-STEM image simulation. This work was financially supported by the Japan Science and Technology Agency (JST) CREST program (JPMJCR20T3), the JST FOREST Program (JPMJFR213X), the JST PRESTO program (JPMJPR23H5), Kakenhi Grants-in-Aid (JP19H00664, JP20H00354, JP20H05664, JP20K14415, JP20H01840, JP20H00127, JP21H05232, JP21H05233, JP21H05234, JP21H05235, JP21H05236, JP22H00280, JP22H00283, JP22K18986, JP22H04957, JP22H05441, JP22KJ2561, JP23K13635, JP23H02052, and JP23H01807) from the Japan Society for the Promotion of Science (JSPS), Sumitomo Foundation Fiscal 2021 Grant for Basic Science Research Projects, Yazaki Memorial Foundation for Science and Technology, Mitsubishi Foundation, Murata Science Foundation Research Grant, and ZE Research Program, IAE (ZE2023B-05).

Conflict of Interest

The authors declare no conflict of interest.

Data Availability Statement

The data that support the findings of this study are available from the corresponding author upon reasonable request.

Keywords

heterobilayers, Janus transition metal dichalcogenides, moiré excitons, moiré superlattices, plasma treatment

Received: November 26, 2023
Revised: January 31, 2024
Published online: March 1, 2024

[1] L. Balents, C. R. Dean, D. K. Efetov, A. F. Young, *Nat. Phys.* **2020**, *16*, 725.
[2] K. F. Mak, J. Shan, *Nat. Nanotechnol.* **2022**, *17*, 686.
[3] D. Huang, J. Choi, C.-K. Shih, X. Li, *Nat. Nanotechnol.* **2022**, *17*, 227.
[4] N. P. Wilson, W. Yao, J. Shan, X. Xu, *Nature* **2021**, *599*, 383.
[5] H. Ago, S. Okada, Y. Miyata, K. Matsuda, M. Koshino, K. Ueno, K. Nagashio, *Sci. Technol. Adv. Mater.* **2022**, *23*, 275.
[6] J. Choi, W.-T. Hsu, L.-S. Lu, L. Sun, H.-Y. Cheng, M.-H. Lee, J. Quan, K. Tran, C.-Y. Wang, M. Staab, K. Jones, T. Taniguchi, K. Watanabe, M.-W. Chu, S. Gwo, S. Kim, C.-K. Shih, X. Li, W.-H. Chang, *Sci. Adv.* **2020**, *6*, eaba8866.
[7] Y. C. Cheng, Z. Y. Zhu, M. Tahir, U. Schwingenschlögl, *EPL Europhys. Lett.* **2013**, *102*, 57001.
[8] Q.-F. Yao, J. Cai, W.-Y. Tong, S.-J. Gong, J.-Q. Wang, X. Wan, C.-G. Duan, J. H. Chu, *Phys. Rev. B* **2017**, *95*, 165401.
[9] F. Li, W. Wei, P. Zhao, B. Huang, Y. Dai, *J. Phys. Chem. Lett.* **2017**, *8*, 5959.
[10] R. Guo, X. Bu, S. Wang, G. Zhao, *New J. Phys.* **2019**, *21*, 113040.
[11] Y. Wang, W. Wei, B. Huang, Y. Dai, *J. Phys. Condens. Matter* **2019**, *31*, 125003.
[12] T. Hu, F. Jia, G. Zhao, J. Wu, A. Stroppa, W. Ren, *Phys. Rev. B* **2018**, *97*, 235404.
[13] C. Xia, W. Xiong, J. Du, T. Wang, Y. Peng, J. Li, *Phys. Rev. B* **2018**, *98*, 165424.
[14] F. Li, W. Wei, H. Wang, B. Huang, Y. Dai, T. Jacob, *J. Phys. Chem. Lett.* **2019**, *10*, 559.
[15] W. Zhou, J. Chen, Z. Yang, J. Liu, F. Ouyang, *Phys. Rev. B* **2019**, *99*, 075160.
[16] L. Dong, J. Lou, V. B. Shenoy, *ACS Nano* **2017**, *11*, 8242.
[17] N. A. Pike, R. Pachter, *J. Phys. Chem. C* **2022**, *126*, 16243.
[18] A. Strasser, H. Wang, X. Qian, *Nano Lett.* **2022**, *22*, 4145.
[19] X. Liu, H. Zeng, G. Wang, X. Cheng, S. A. Yang, H. Zhang, *Phys. Chem. Chem. Phys.* **2022**, *24*, 11743.
[20] H. Jin, T. Wang, Z.-R. Gong, C. Long, Y. Dai, *Nanoscale* **2018**, *10*, 19310.
[21] X. Ma, X. Wu, H. Wang, Y. Wang, *J. Mater. Chem. A* **2018**, *6*, 2295.
[22] C. Long, Y. Dai, Z.-R. Gong, H. Jin, *Phys. Rev. B* **2019**, *99*, 115316.
[23] H. Guo, X. Zhang, G. Lu, *Sci. Adv.* **2022**, *8*, eabp9757.
[24] Y. Liang, J. Li, H. Jin, B. Huang, Y. Dai, *J. Phys. Chem. Lett.* **2018**, *9*, 2797.
[25] B. Song, L. Liu, C. Yam, *J. Phys. Chem. Lett.* **2019**, *10*, 5564.
[26] A.-Y. Lu, H. Zhu, J. Xiao, C.-P. Chuu, Y. Han, M.-H. Chiu, C.-C. Cheng, C.-W. Yang, K.-H. Wei, Y. Yang, Y. Wang, D. Sokaras, D. Nordlund, P. Yang, D. A. Muller, M.-Y. Chou, X. Zhang, L.-J. Li, *Nat. Nanotechnol.* **2017**, *12*, 744.
[27] J. Zhang, S. Jia, I. Kholmanov, L. Dong, D. Er, W. Chen, H. Guo, Z. Jin, V. B. Shenoy, L. Shi, J. Lou, *ACS Nano* **2017**, *11*, 8192.
[28] Y. Qin, M. Sayyad, A. R.-P. Montblanch, M. S. G. Feuer, D. Dey, M. Blei, R. Sailus, D. M. Kara, Y. Shen, S. Yang, A. S. Botana, M. Atature, S. Tongay, *Adv. Mater.* **2022**, *34*, 2106222.
[29] C. W. Jang, W. J. Lee, J. K. Kim, S. M. Park, S. Kim, S.-H. Choi, *NPG Asia Mater.* **2022**, *14*, 1.
[30] J. Schmeink, V. Musytschuk, E. Pollmann, S. Sleziona, A. Maas, P. Kratzer, M. Schleberger, *Nanoscale* **2023**, *15*, 10834.
[31] Y.-C. Lin, C. Liu, Y. Yu, E. Zarkadoula, M. Yoon, A. A. Puretzky, L. Liang, X. Kong, Y. Gu, A. Strasser, H. M. I. Meyer, M. Lorenz, M. F. Chisholm, I. N. Ivanov, C. M. Rouleau, G. Duscher, K. Xiao, D. B. Geohegan, *ACS Nano* **2020**, *14*, 3896.
[32] T. Zheng, Y.-C. Lin, Y. Yu, P. Valencia-Acuna, A. A. Puretzky, R. Torsi, C. Liu, I. N. Ivanov, G. Duscher, D. B. Geohegan, Z. Ni, K. Xiao, H. Zhao, *Nano Lett.* **2021**, *21*, 931.
[33] H. Li, Y. Qin, B. Ko, D. B. Trivedi, D. Hajra, M. Y. Sayyad, L. Liu, S.-H. Shim, H. Zhuang, S. Tongay, *Adv. Mater.* **2020**, *32*, 2002401.
[34] Z. Gan, I. Paradisanos, A. Estrada-Real, J. Picker, E. Najafidehaghani, F. Davies, C. Neumann, C. Robert, P. Wiecha, K. Watanabe, T. Taniguchi, X. Marie, J. Biskupek, M. Mundszinger, R. Leiter, U. Kaiser, A. V. Krasheninnikov, B. Urbaszek, A. George, A. Turchanin, *Adv. Mater.* **2022**, *34*, 2205226.
[35] K. Zhang, Y. Guo, Q. Ji, A.-Y. Lu, C. Su, H. Wang, A. A. Puretzky, D. B. Geohegan, X. Qian, S. Fang, E. Kaxiras, J. Kong, S. Huang, *J. Am. Chem. Soc.* **2020**, *142*, 17499.
[36] D. B. Trivedi, G. Turgut, Y. Qin, M. Y. Sayyad, D. Hajra, M. Howell, L. Liu, S. Yang, N. H. Patoary, H. Li, M. M. Petrić, M. Meyer, M. Kremser, M. Barbone, G. Soavi, A. V. Stier, K. Müller, S. Yang, I. S. Esqueda, H. Zhuang, J. J. Finley, S. Tongay, *Adv. Mater.* **2020**, *32*, 2006320.
[37] T. Zheng, Y.-C. Lin, N. Rafizadeh, D. B. Geohegan, Z. Ni, K. Xiao, H. Zhao, *ACS Nano* **2022**, *16*, 4197.
[38] K. Zhang, Y. Guo, D. T. Larson, Z. Zhu, S. Fang, E. Kaxiras, J. Kong, S. Huang, *ACS Nano* **2021**, *15*, 14394.
[39] M. Kaneda, W. Zhang, Z. Liu, Y. Gao, M. Maruyama, Y. Nakanishi, H. Nakajo, S. Aoki, K. Honda, T. Ogawa, K. Hashimoto, T. Endo, K. Aso, T. Chen, Y. Oshima, Y. Yamada-Takamura, Y. Takahashi, S. Okada, T. Kato, Y. Miyata, *ACS Nano* **2024**, *18*, 2772.
[40] M. Xia, B. Li, K. Yin, G. Capellini, G. Niu, Y. Gong, W. Zhou, P. M. Ajayan, Y.-H. Xie, *ACS Nano* **2015**, *9*, 12246.
[41] S. Li, Y.-C. Lin, W. Zhao, J. Wu, Z. Wang, Z. Hu, Y. Shen, D.-M. Tang, J. Wang, Q. Zhang, H. Zhu, L. Chu, W. Zhao, C. Liu, Z. Sun, T. Taniguchi, M. Osada, W. Chen, Q.-H. Xu, A. T. S. Wee, K. Suenaga, F. Ding, G. Eda, *Nat. Mater.* **2018**, *17*, 535.
[42] M. M. Petrić, M. Kremser, M. Barbone, Y. Qin, Y. Sayyad, Y. Shen, S. Tongay, J. J. Finley, A. R. Botello-Méndez, K. Müller, *Phys. Rev. B* **2021**, *103*, 035414.
[43] H. Suzuki, Y. Liu, M. Misawa, C. Nakano, Y. Wang, R. Nakano, K. Ishimura, K. Tsuruta, Y. Hayashi, *Nano Lett.* **2023**, *23*, 4533.
[44] X. Wan, E. Chen, J. Yao, M. Gao, X. Miao, S. Wang, Y. Gu, S. Xiao, R. Zhan, K. Chen, Z. Chen, X. Zeng, X. Gu, J. Xu, *ACS Nano* **2021**, *15*, 20319.
[45] H. Li, X. Duan, X. Wu, X. Zhuang, H. Zhou, Q. Zhang, X. Zhu, W. Hu, P. Ren, P. Guo, L. Ma, X. Fan, X. Wang, J. Xu, A. Pan, X. Duan, *J. Am. Chem. Soc.* **2014**, *136*, 3756.
[46] F. A. Nugera, P. K. Sahoo, Y. Xin, S. Ambardar, D. V. Voronine, U. J. Kim, Y. Han, H. Son, H. R. Gutiérrez, *Small* **2022**, *18*, 2106600.
[47] R. Rong, Y. Liu, X. Nie, W. Zhang, Z. Zhang, Y. Liu, W. Guo, *Adv. Sci.* **2023**, *10*, 2206191.
[48] T. Li, S. Jiang, L. Li, Y. Zhang, K. Kang, J. Zhu, K. Watanabe, T. Taniguchi, D. Chowdhury, L. Fu, J. Shan, K. F. Mak, *Nature* **2021**, *597*, 350.

[49] C. Jin, E. C. Regan, A. Yan, M. Iqbal Bakti Utama, D. Wang, S. Zhao, Y. Qin, S. Yang, Z. Zheng, S. Shi, K. Watanabe, T. Taniguchi, S. Tongay, A. Zettl, F. Wang, *Nature* **2019**, *567*, 76.
[50] Y. Ding, N. Zhou, L. Gan, X. Yan, R. Wu, I. H. Abidi, A. Waleed, J. Pan, X. Ou, Q. Zhang, M. Zhuang, P. Wang, X. Pan, Z. Fan, T. Zhai, Z. Luo, *Nano Energy* **2018**, *49*, 200.
[51] X. Li, M.-W. Lin, J. Lin, B. Huang, A. A. Puretzky, C. Ma, K. Wang, W. Zhou, S. T. Pantelides, M. Chi, I. Kravchenko, J. Fowlkes, C. M. Rouleau, D. B. Geohegan, K. Xiao, *Sci. Adv.* **2016**, *2*, e1501882.
[52] M. S. G. Feuer, A. R.-P. Montblanch, M. Y. Sayyad, C. M. Purser, Y. Qin, E. M. Alexeev, A. R. Cadore, B. L. T. Rosa, J. Kerfoot, E. Mostaani, R. Kalęba, P. Kolari, J. Kopaczek, K. Watanabe, T. Taniguchi, A. C. Ferrari, D. M. Kara, S. Tongay, M. Atatüre, *ACS Nano* **2023**, *17*, 7326.
[53] S. Kumar, A. Kaczmarczyk, B. D. Gerardot, *Nano Lett.* **2015**, *15*, 7567.
[54] K. Parto, S. I. Azzam, K. Banerjee, G. Moody, *Nat. Commun.* **2021**, *12*, 3585.
[55] K. Tran, G. Moody, F. Wu, X. Lu, J. Choi, K. Kim, A. Rai, D. A. Sanchez, J. Quan, A. Singh, J. Embley, A. Zepeda, M. Campbell, T. Autry, T. Taniguchi, K. Watanabe, N. Lu, S. K. Banerjee, K. L. Silverman, S. Kim, E. Tutuc, L. Yang, A. H. MacDonald, X. Li, *Nature* **2019**, *567*, 71.
[56] K. L. Seyler, P. Rivera, H. Yu, N. P. Wilson, E. L. Ray, D. Mandrus, J. Yan, W. Yao, X. Xu, *Nature* **2019**, *567*, 66.
[57] X. Xu, X. Jiang, Q. Gao, L. Yang, X. Sun, Z. Wang, D. Li, B. Cui, D. Liu, *Phys. Chem. Chem. Phys.* **2022**, *24*, 29882.
[58] M. Angeli, G. R. Schleder, E. Kaxiras, *Phys. Rev. B* **2022**, *106*, 235159.
[59] H. Naito, Y. Makino, W. Zhang, T. Ogawa, T. Endo, T. Sannomiya, M. Kaneda, K. Hashimoto, H. E. Lim, Y. Nakanishi, K. Watanabe, T. Taniguchi, K. Matsuda, Y. Miyata, *Nanoscale Adv.* **2023**, *5*, 5115.
[60] K. S. Novoselov, D. Jiang, F. Schedin, T. J. Booth, V. V. Khotkevich, S. V. Morozov, A. K. Geim, *Proc. Natl. Acad. Sci.* **2005**, *102*, 10451.
[61] Y. Morikawa, K. Iwata, K. Terakura, *Appl. Surf. Sci.* **2001**, *169–170*, 11.
[62] STATE Documentation, https://state-doc.readthedocs.io/en/latest/ (accessed: April 2023).
[63] P. Hohenberg, W. Kohn, *Phys. Rev.* **1964**, *136*, B864.
[64] W. Kohn, L. J. Sham, *Phys. Rev.* **1965**, *140*, A1133.
[65] J. P. Perdew, K. Burke, M. Ernzerhof, *Phys. Rev. Lett.* **1996**, *77*, 3865.
[66] V. R. Cooper, *Phys. Rev. B* **2010**, *81*, 161104.
[67] K. Lee, É. D. Murray, L. Kong, B. I. Lundqvist, D. C. Langreth, *Phys. Rev. B* **2010**, *82*, 081101.
[68] D. Vanderbilt, *Phys. Rev. B* **1990**, *41*, 7892.
[69] M. Otani, O. Sugino, *Phys. Rev. B* **2006**, *73*, 115407.
[70] M. Maruyama, K. Nagashio, S. Okada, *ACS Appl. Electron. Mater.* **2020**, *2*, 1352.